White-light femtosecond Lidar at 100 TW power level — **Source link** ⬏

Massimo Petrarca, Stefano Henin, Nicolas Berti, Mary Matthews ...+9 more authors

Institutions: University of Geneva, National Institute for Space Research

Related papers:

- Femtosecond filamentation in transparent media

- Ultrashort filaments of light in weakly ionized, optically transparent media

- Self-channeling of high-peak-power femtosecond laser pulses in air

- Advances in intense femtosecond laser filamentation in air

- Conversion of high-power femtosecond laser pulse to supercontinuum in atmospheric air

RAPID COMMUNICATION

White-light femtosecond Lidar at 100 TW power level

**M. Petrarca · S. Henin · N. Berti · M. Matthews ·
J. Chagas · J. Kasparian · J.-P. Wolf · G. Gatti ·
G. Di Pirro · M.-P. Anania · M. Ferrario · A. Ghigo**

Abstract We characterized the white-light supercontinuum emission by a sub-petawatt laser system in the atmosphere via light detection and ranging measurements. As much as 1 J of supercontinuum is generated in the atmosphere, corresponding to a conversion efficiency of 30 %. This generation occurs at altitudes below 100 m. The high initial beam intensity results in the saturation of the number of self-guided filaments. Therefore, the "photon bath" surrounding the filaments strongly contributes to the white-light generation. These finding is well reproduced by numerical simulations based on the experimental parameters.

1 Introduction

Several recent developments on the remote sensing of atmospheric species by light detection and ranging (Lidar) have involved ultrashort and intense laser beams. The high power of the propagated laser beam allows nonlinear effects to occur such as single-beam coherent antistokes

Raman scattering (CARS) [1–3], plasma fluorescence [4, 5], and even atmospheric lasing [6–8].

Most of these techniques can benefit of laser filamentation [9–12]. Filamentation occurs at laser powers above a critical value (≥3 GW in air at 800 nm). It is due to a dynamic balance between Kerr lens self-focusing of the beam (due to the transverse spatial intensity profile) and defocusing by both the laser-generated plasma and the negative higher-order Kerr terms [13]. Filaments convey intensities around 50 TW/cm^2 [14] and can propagate over tens to hundreds of meters in adequate conditions [15–17]. The high intensity and length of laser filaments allow efficient self-phase modulation (SPM), a temporal counterpart of the Kerr effect, resulting in a "white-light" supercontinuum ranging from the ultraviolet to the mid-infrared [18, 19]. About two-thirds of the continuum is emitted as "conical emission," i.e., as a cone with an half-angle ranging from 1.5 to 7.5 mrad for wavelengths from 700 to 250 nm, respectively [20–22].

At even higher powers (≥100 TW), ultrashort laser beams generate hundreds of filaments. Their transverse density is, however, limited to ∼10 cm^{-2} across the beam profile [23]. Consequently, most of the beam energy propagates in a "photon bath" surrounding the filaments, with intensity in the TW/cm^2 range, sufficient to contribute substantially to the beam nonlinearity, including supercontinuum generation [24].

The spectrum covered by the supercontinuum is governed by the temporal pulse shape and the nonlinear refractive index of the air. Unlike plasma emission, it is therefore coherent and free from molecular or atomic lines. This property makes it particularly suitable for spectroscopic applications. It has been proposed as a collimated light source to measure simultaneously the absorptions of all the species present along the laser path beyond the

M. Petrarca · S. Henin · N. Berti · M. Matthews · J. Chagas ·
J. Kasparian · J.-P. Wolf (✉)
GAP, Université de Genève, Chemin de Pinchat 22,
1211 Genève 4, Switzerland
e-mail: Jean-Pierre.Wolf@unige.ch

M. Petrarca · G. Gatti · G. Di Pirro · M.-P. Anania ·
M. Ferrario · A. Ghigo
INFN-LNF, Via E. Fermi, 40, 00044 Frascati, Rome, Italy

J. Chagas
Centro de Previsão do Tempo e Estudos Climáticos-CPTEC,
Instituto Nacional de Pesquisas Espaciais-INPE, Cachoeira
Paulista, SP, Brazil

filamentation region, an approach known as "white-light DIAL" (Differential Absorption Lidar) or "multi-DIAL" [9, 25–28]. Multi-DIAL can be seen as a generalization of standard DIAL, in which a wavelength pair is matched to the spectrum of the predetermined species to detect: one wavelength absorbed by the molecule to detect and the other used as reference. Offering a unique multi-species measurement capability, multi-DIAL would be mostly attractive for analyzing species emitted by, e.g., industrial incidents, leakages, fires, as well as for unknown aerosols, since it does not require any a priori knowledge of the species present in the air.

In order to assess the potential of the multi-DIAL technique, the evolution of the white-light Lidar signal intensity with laser power is a key information. Most of the previous results were obtained at powers on the TW level [25–28]. However, laser technology allows now increasing the power level by orders of magnitude. Simultaneously, the footprint, compactness, and robustness of laser systems steadily improve, raising the prospect to perform field experiments at extreme power levels. Here, we present the first femtosecond white-light Lidar signals from a sub-PW class laser system, the Frascati laser for acceleration, and multi-disciplinary experiments (FLAME) laser of the SPARC_LAB facility [29] at the INFN-Frascati [30].

2 Experimental setup

FLAME is a Ti:Sa chirped pulse amplification (CPA) laser chain providing up to 5 J, 200 TW pulses of 25 fs duration, at a repetition rate of 10 Hz, and a 40-nm bandwidth centered at 800 nm. The pulse energy was adjusted by rotating a half-wave plate associated with a polarizer, placed before the grating compressor, while its duration was controlled by tailoring the pulse using an acousto-optic modulator (Fastlite Dazzler) [31] located at the exit of the pulse stretcher and by detuning the compressor. In the present experiments, pulse durations from 30 fs to 5 ps were achievable, with either chirp sign. According to a common convention, the pulse durations corresponding to negative chirps are written in the following as negative numbers. At the exit of the compressor vacuum chamber, the laser was directed by a single mirror into the sky, at an angle of $\sim 60°$ from vertical, as a collimated beam of ~ 10 cm diameter (Fig. 1). Measurement time slots were specified and allocated in agreement with the air traffic control division of the Roma-Ciampino airport.

During its propagation in the atmosphere, the FLAME laser beam produced a strong supercontinuum by filamentation. The resulting "white" beam undergoes Rayleigh and Mie scattering by atmospheric molecules (and sub-wavelength particles) and by larger particles, respectively.
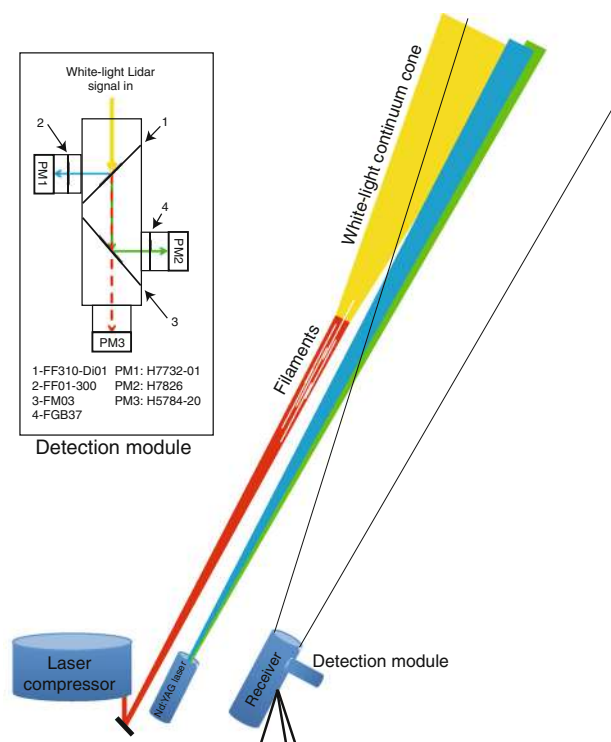

Fig. 1 a Schematic layout of the Lidar experiment. The receiver telescope is located ~ 90 cm and 1 m below the FLAME and reference Nd:YAG laser beams. The beam axes lie at a distance of 12 cm to each other. The layout of the detection module is detailed in the inset

Its backscattered fraction was collected in a Lidar configuration by a 200-mm aperture Newtonian telescope of $f = 1,190$ mm focal length and UV-enhanced Al + MgF$_2$ coated optics.

As sketched in the inset of Fig. 1, the collected light was separated into three spectral channels and recorded time resolved, providing distance resolution. The visible light (390–620 nm), was selected by a Thorlabs Cold Mirror FM03 and a Thorlabs FGB37 colored glass filter and recorded by a Hamamatsu H7826 photomultiplier (PM2). Ultraviolet light (255–290 nm) was separated by Semrock filters FF310-Di01 and FF01-300 and detected by a Hamamatsu H7732-01 photomultiplier (PM1). The remaining near-IR fundamental light of the FLAME laser was detected on a Hamamatsu H5784-20 (PM3) photomultiplier and used to align the telescope on the latter beam. The signals from the photomultipliers were digitized and recorded by three 8-bit acquisition boards (National Instrument PXI 5154: 2GS/s, 1 GHz and PXI 5114: 250Ms/s, 125 MHz) and averaged over 1,000 laser pulses.

Calibration measurements were taken using the same receiver system with an auxiliary Nd:YAG laser (Quantel CFR200) delivering up to 45 mJ at 266 nm and 150 mJ at 532 nm in a co-propagating geometry. The following procedure ensured the overlap between the laser beams and

the telescope field of view: First, the telescope was aligned on the FLAME beam by optimizing the Lidar signal from PM3. Then, the Nd:YAG beams were steered to optimize the corresponding Lidar signals, ensuring the spatial overlap with the FLAME beam. Both the Nd:YAG and FLAME beams were therefore emitted parallel, with an off-axis distance of ~ 0.9 and 1 m from the telescope axis, respectively, and a distance of 12 cm from each other.

3 Results and discussion

Figure 2 displays the Lidar signals, i.e., the range-resolved backscattering signals, in both the UV and the visible fractions of the supercontinuum, for 3 values of initial chirp of the FLAME laser: $-34{,}134$ fs^2, $-18{,}963$ fs^2, and $+18{,}963$ fs^2, corresponding to pulse durations of -3.15 ps, -1.75 ps, and $+1.75$ ps, respectively. Linear Lidar signals from the Nd:YAG reference laser are also displayed in each spectral range.

The first striking result is that the strongest Lidar signal in the visible channel, hence the most efficient supercontinuum generation in that spectral range, is obtained for the positive chirp. This trend is consistent with our previous horizontal propagation measurements with 100 TW-class lasers at FZD-Rossendorf [24], although this measurement was restricted to much shorter propagation distances, below 42 m.

This result is, however, counter-intuitive because one would expect that, because of normal dispersion in air, a negatively chirped pulse would recompress during its propagation, resulting in a higher intensity and thus more favorable to nonlinear effects like filamentation. Our results can, however, be understood by considering that, as mentioned above, at sub-PW powers, the photon bath bears

enough intensity ($\geq \sim 1$ TW/cm^2) to substantially contribute to the supercontinuum by self-phase modulation [24]. For a positive nonlinear refractive index (e.g., $n_2 = 1.2 \times 10^{-19}$ cm^2/W in air [13]), SPM shifts the leading edge of the pulse to longer wavelengths and the trailing edge to shorter wavelengths. In positively chirped pulses, the leading edge already bears the longer wavelengths, and the shorter wavelengths are on the trailing edge. This time-dependent frequency offset within the pulse is therefore reinforced by SPM. On the other hand, if the pulse is negatively chirped, SPM red shifts its blue-shifted leading edge and blue shifts its red-shifted trail, thus reducing the spectral width. A positive chirp is therefore more favorable for spectral broadening. Our results show that, under our conditions and in the visible part of the supercontinuum, this effect overrides the pulse temporal recompression or spreading due to group-velocity dispersion.

These conditions are not fulfilled anymore in the case of the UV generation, where efficient third-harmonic generation (THG, up to 0.5 % conversion efficiency) occurs and subsequently broadens via self- and cross-phase modulation [37]. In this situation, the phase-matching mismatch due to group-velocity dispersion between the UV and the IR part of the continuum is such that a negative chirp becomes more favorable, as displayed by the results in Fig. 2a.

In order to locate the position of the filaments and the associated supercontinuum generation, we compared the Lidar signal from FLAME and the reference nanosecond Nd:YAG. In particular, if white-light supercontinuum was generated only after a certain distance (e.g., after the filamentation onset), then a remote source term should displace the maximum of the white-light Lidar signals as compared to the reference laser. This situation was not observed under our experimental conditions, namely chirps

Fig. 2 Range-resolved backscattering light (Lidar signal) in **a** UV (255–290 nm) and **b** visible (390–620 nm), for three chirp values of the FLAME laser, corresponding to pulse durations of -3.15, -1.75, and $+1.75$ ps
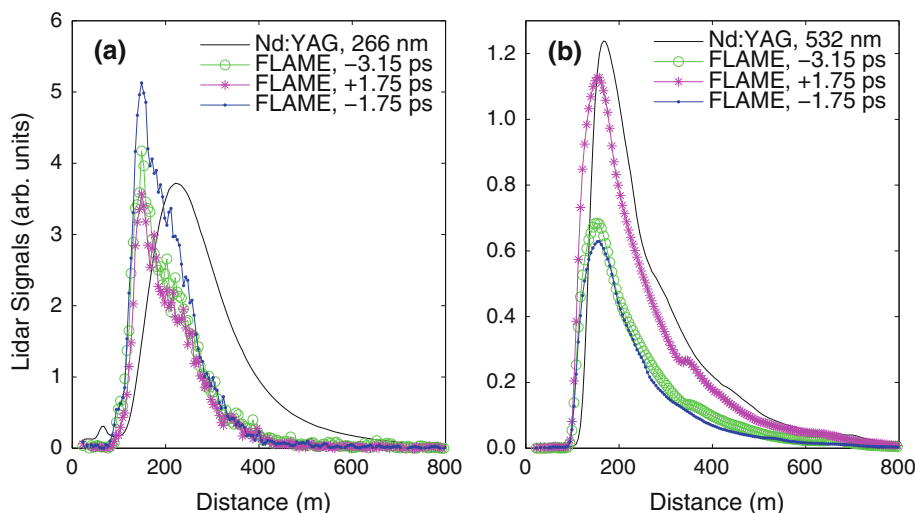
up to 3.15 ps and 10 cm beam diameter. Rather, the intensity dependence on distance R was characteristic of a standard Lidar signal, with a blind zone at short distances due to the overlap function $\xi(R, \lambda)$ [32] between the transmitted laser beam and the field of view of the receiver telescope [33, 34], followed by an overall decrease with distance due to the decreasing $1/R^2$ solid angle of the receiver and to atmospheric extinction. More precisely, in the limit of single scattering events, the linearly backscattered intensity follows the Lidar equation [35, 36]:

$$M(R,\lambda) = M_0(\lambda)\frac{A_0}{R^2}\beta(R,\lambda)\Delta R\,\xi(R,\lambda)\exp\left[-2\int_0^R \alpha(R,\lambda)dR\right]$$
(1)

where: $M_0(\lambda)$ is the number of photons emitted by the laser,
   A_0 the area of the receiver telescope,
   ΔR the spatial resolution of the system, essentially determined by the laser pulse duration τ, $\Delta R = c\tau/2$, and the response time of the acquisition electronics,
   $\xi(R, \lambda)$ the detection efficiency, including the overlap function between the laser and the telescope field of view,
   $\beta(R, \lambda)$ the volume backscattering coefficient, and
   $\alpha(R, \lambda)$ the total atmospheric extinction coefficient.

The aerosol concentration in the atmosphere is included in Eq. (1) via two scattering parameters: the volume backscattering coefficient β and the extinction α. The extinction stems from both Rayleigh–Mie scattering α_{RM} and specific molecular absorption α_A of the different species present in the atmosphere. The α_{RM} extinction coefficient, like β, is integrated over the size distribution, shape and composition (via the refractive index) of the aerosol particles. In our experiments, a low altitude haze layer is clearly observed up to 700 m. This altitude corresponds to the planetary boundary layer (PBL), i.e., the lower layer of the atmosphere, the flow of which is influenced by the ground surface roughness. The α_{RM} and β_{RM} values could be estimated by the measurement of the visibility range [37] at the time of the experiments (10 km, data from Ciampino Airport): α_{RM} (visible) $= 4 \times 10^{-4}$ m^{-1}, α_{RM} (UV) $= 9 \times 10^{-4}$ m^{-1}, β_{RM} (visible) $= 7 \times 10^{-6}$ m^{-1} sr^{-1}, and β_{RM} (UV) $= 3 \times 10^{-5}$ m^{-1} sr^{-1}. The absorption at 266 nm due to the background ozone concentration was low enough to be neglected.

Comparing the Lidar signal amplitudes for the backward-emitted supercontinuum and the reference Nd:YAG laser allowed us to determine the energy contained in the supercontinuum and the related conversion efficiency. Lidar signals of amplitudes identical to the supercontinuum generated in the visible (chirped with +1.75 ps) were obtained for Nd:YAG laser pulses of energies reduced to 3 mJ at 532 nm.

It is particularly interesting to compare these spectral densities to the one measured on a similar laser chain (Amplitude DRACO laser, 3 J, 30 fs) at the FZD-Rossendorf [23, 24]. This latter experiment exhibited an energy conversion of up to 30 % into the continuum ($\lambda < 765$ and $\lambda > 845$ nm), representing about 1 J of white light in the case of unchirped pulses. Since the spectral distribution exponentially decreased on both sides of the spectrum with a slope of roughly a decade every 100 nm, we estimated from the original data that the energy contained in the [390–620 nm] interval at the FZD-Rossendorf after 42 m horizontal propagation amounts to about 8 mJ, i.e., a value similar to that obtained in the present Lidar experiment (3 mJ) with the FLAME laser. The slightly lower yield in the latter case can be attributed to the longer pulse duration induced by the chirp. This suggests that in the present experiment, the major part of the supercontinuum was generated at low altitude (<100 m), into the blind zone of our Lidar arrangement. Such finding is consistent with the fact that the observed Lidar signals follow the linear Lidar equation, without the need to introduce a source term corresponding to white-light generation due to the presence of filaments at higher altitude. More details about the effect of the source term in the Lidar Eq. (1) are presented in [38].

To further investigate this behavior, we simulated the Lidar signals by solving the Lidar Eq. (1), using all the instrumental parameters. The agreement with experiments was first checked on the elastic Lidar signals from the reference Nd:YAG laser. The accuracy of the simulation is limited by the fluctuations of the aerosol concentration within the light haze layer. Due to the lack of information on these fluctuations, we modeled Mie scattering using α_{RM} and β_{RM} values constant with altitude.

Figure 3 displays the results of the optimized simulations as compared to the measured data (log scale). As can be seen, the inhomogeneity within the PBL as well as its fluctuation between different measurements do not allow for quantitative comparison. However, reasonable fits of the geometrical compression region, i.e., the distance range (0–250 m) where the telescope field of view does not fully overap the laser beam [32] could only be obtained by assuming filaments generated below 100 m, with a divergence of 3 ± 0.5 mrad (half angle), which is consistent with the conical emission in the visible [22]. The uncertainty on the supercontinuum divergence corresponds to the range over which the simulated Lidar signal matched the experimental one reasonably well. On the other hand, the lack of signal below 150 m only allows an indirect estimation of the filament onset altitude, via the observed overlap function between the telescope and the laser, therefore allowing only an upper limit.

While the Lidar signals corresponding to the visible part of the supercontinuum and to the Nd:YAG laser at 532 nm

Fig. 3 Experimental and simulated Lidar signals from **a** 3 mJ frequency-doubled Nd:YAG at 532 nm, and **b**–**d** white-light in the visible for three chirping values of the FLAME laser. Each frame is labeled by the corresponding laser pulse duration
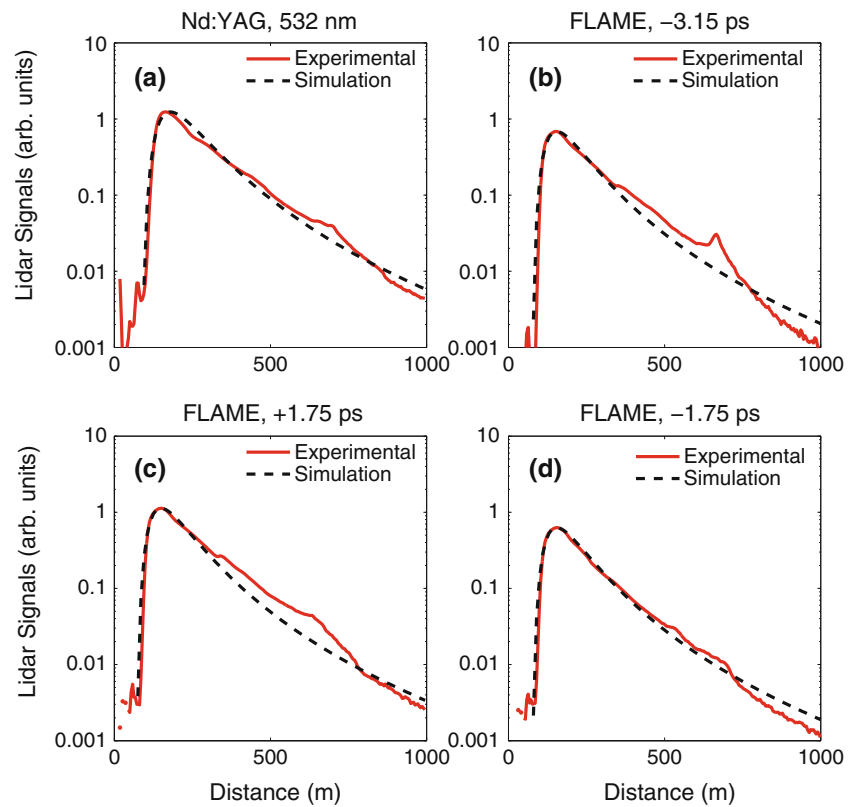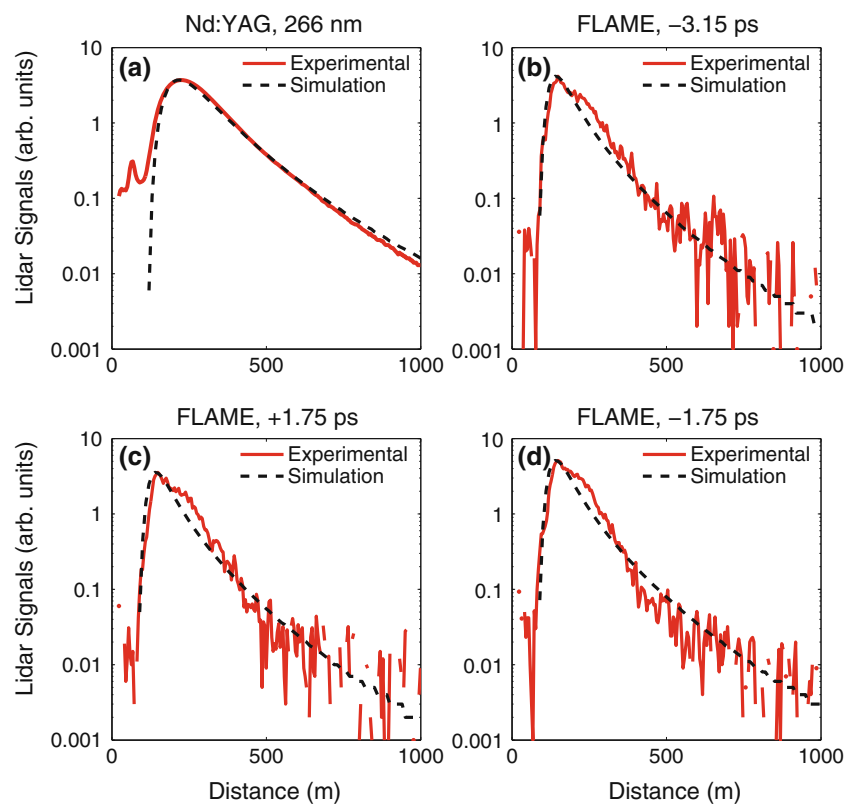
Fig. 4 Experimental and simulated Lidar signals from **a** the Nd:YAG at 266 nm and **b**–**d** white-light in the UV for three chirping values of the FLAME laser. Each frame is labeled by the corresponding laser pulse duration

look pretty much alike, the situation is different in the UV (Fig. 4). This difference evidences the different geometries of the visible and UV parts of the supercontinuum emission. More precisely, the detected UV supercontinuum Lidar signals start at lower altitudes (150 m) and decay with a much steeper slope than in the visible. Again, fits using Eq. (1) allowed to attribute this behavior to the geometrical overlap between the UV emission and the receiving optics. In the UV, the supercontinuum cone (7.5 mrad) [22] containing 80 % of the total energy encompasses a narrower cone including third-harmonic generation [39]. Due to the wide angle of the UV conical emission, the backscattered light penetrates the 3 mrad field of view of the telescope at shorter distance, and since the receiver acceptance angle is smaller than the outer cone of the UV emission, the spatial overlap function $\xi(R, \lambda)$ rapidly decays with distance.

In our experimental configuration, even though the supercontinuum emission is efficient (comparable to the 1 J of white light measured at the FZD-Rossendorf), it is mainly produced below 100 meters, even at the longest available pulse durations (5 ps). This result contrasts with previous experiments carried out at lower power (few TW) with the Teramobile [40, 41], where the filamentation onset could successfully be controlled by temporal focusing, i.e., by tuning the initial chirp. In particular, the filamentation onset could be shifted to a distance of 250 m by stretching the pulse duration up to 6 ps [41]. However, the initial peak intensity of these pulses corresponded only to 2×10^9 W/cm^2. In the present case of a 3 J laser and a beam diameter of 10 cm, reducing the intensity to the same level would require about 20 ps duration, which could not be achieved with the FLAME compressor. Moreover, during its nonlinear propagation, the pulse would recompress up to intensities where congestion limits the number of filaments, and the whole pulse including photon bath would refocus. In order to better characterize propagation at the sub-PW level, direct horizontal measurements over several hundred meters are required. The photon bath of high energy and high power laser beam can play an important role in practical applications such as laser promoted particle formation [42–44], and therefore, it deserves further investigation. It also has to be taken into account in analyzing Lidar signals based on the supercontinuum. This includes considering the actual emission geometry of the white light, which cannot be treated as a Y-shaped beam on large beams as it is the case in lower power beams generating a single filament [32].

4 Conclusion

As a conclusion, we have characterized the supercontinuum generation from very high power (sub-PW) laser pulses

by performing white-light Lidar measurements. Contrary to observations at lower power, the high intensity in the beam from the laser exit on allows efficient supercontinuum generation at low altitude ($\leq$100 m) from the photon bath, a behavior that can be well reproduced by numerical simulations. In order to shift the filamentation onset to larger distances, the beam would have to expand to large apertures and/or the pulse should be chirped on non-conventional timescales (several tens of ps). Furthermore, the emission geometry influences Lidar signals based on the white-light supercontinuum and therefore has to be carefully characterized.

References

1. D. Pestov, R.K. Murawski, G.O. Ariunbold, X. Wang, M.C. Zhi, A.V. Sokolov, V.A. Sautenkov, Y.V. Rostovtsev, A. Dogariu, Y. Huang, M.O. Scully, Science **316**, 265 (2007)
2. A. Natan, J.M. Levitt, L. Graham, O. Katz, Y. Silberberg, Appl. Phys. Lett. **100**, 051111 (2012)
3. H.W. Li, D.A. Harris, B. Xu, P.J. Wrzesinski, V.V. Lozovoy, M. Dantus, Opt. Express **16**, 5499 (2008)
4. H.L. Xu, G. Méjean, W. Liu, Y. Kamali, J.F. Daigle, A. Azarm, P.T. Simard, P. Mathieu, G. Roy, J.R. Simard, S.L. Chin, Appl. Phys. B **87**, 151 (2007)
5. Q. Luo, H.L. Xu, S.A. Hosseini, J.F. Daigle, F. Theberge, M. Sharifi, S.L. Chin, Appl. Phys. B **82**, 105 (2006)
6. A. Dogariu, J.B. Michael, M.O. Scully, R.B. Miles, Science **331**, 442 (2011)
7. D. Kartashov, S. Alisauskas, G. Andriukaitis, A. Pugzlys, M. Shneider, A. Zheltikov, S.L. Chin, A. Baltuska, Phys. Rev. A **86**, 033831 (2012)
8. Q. Luo, W. Liu, S.L. Chin, Appl. Phys. B **76**, 337 (2003)
9. J. Kasparian, M. Rodriguez, G. Méjean, J. Yu, E. Salmon, H. Wille, R. Bourayou, S. Frey, Y.-B. André, A. Mysyrowicz, R. Sauerbrey, J.-P. Wolf, L. Wöste, Science **301**, 61 (2003)
10. A. Couairon, A. Mysyrowicz, Phys. Rep. **44**, 47 (2007)
11. L. Bergé, S. Skupin, R. Nuter, J. Kasparian, J.-P. Wolf, Rep. Prog. Phys. **70**, 1633 (2007)
12. S.L. Chin, T.-J. Wang, C. Marceau, J. Wu, J.S. Liu, O. Kosareva, N. Panov, Y.P. Chen, J.-F. Daigle, S. Yuan, A. Azarm, W.W. Liu, T. Seideman, H.P. Zeng, M. Richardson, R. Li, Z.Z. Xu, Laser Phys. **22**, 1–53 (2012)
13. P. Béjot, E. Hertz, J. Kasparian, B. Lavorel, J.P. Wolf, O. Faucher, Phys. Rev. Lett. **106**, 243902 (2011)
14. J. Kasparian, R. Sauerbrey, S.L. Chin, Appl. Phys. B **71**, 877–879 (2000)
15. B. La Fontaine, F. Vidal, Z. Jiang, C.Y. Chien, D. Comtois, A. Desparois, T.W. Johnson, J.-C. Kieffer, H. Pépin, Phys. Plasmas **6**, 1615–1621 (1999)
16. G. Méchain, C.D'. Amico, Y.-B. André, S. Tzortzakis, M. Franco, B. Prade, A. Mysyrowicz, A. Couairon, E. Salmon, R. Sauerbrey, Opt. Commun. **247**, 171–180 (2005)
17. M. Durand, A. Houard, B. Prade, A. Mysyrowicz, A. Durécu, B. Moreau, D. Fleury, O. Vasseur, H. Borchert, K. Diener,

R. Schmitt, F. Théberge, M. Chateauneuf, J.-F. Daigle, J. Dubois, Opt. Express **21**, 26836–26845 (2013)

18. J. Kasparian, R. Sauerbrey, D. Mondelain, S. Niedermeier, J. Yu, J.-P. Wolf, Y.-B. André, M. Franco, B. Prade, A. Mysyrowicz, S. Tzortzakis, M. Rodriguez, H. Wille, L. Wöste, Opt. Lett. **25**, 1397–1399 (2000)

19. F. Théberge, M. Châteauneuf, V. Ross, P. Mathieu, J. Dubois, Opt. Lett. **33**, 2515–2517 (2008)

20. E.T.J. Nibbering, P.F. Curley, G. Grillon, B.S. Prade, M.A. Franco, F. Salin, A. Mysyrowicz, Opt. Lett. **21**, 62–64 (1996)

21. O.G. Kosareva, V.P. Kandidov, A. Brodeur, C.Y. Chen, S.L. Chin, Opt. Lett. **22**, 1332–1334 (1997)

22. P. Maioli, R. Salamé, N. Lascoux, E. Salmon, P. Béjot, J. Kasparian, J.-P. Wolf, Opt. Express **17**, 4726–4731 (2009)

23. S. Henin, Y. Petit, J. Kasparian, J.-P. Wolf, A. Jochmann, S.D. Kraft, S. Bock, U. Schramm, R. Sauerbrey, W.M. Nakaema, K. Stelmaszczyk, P. Rohwetter, L. Wöste, C.L. Soulez, S. Mauger, L. Bergé, S. Skupin, Appl. Phys. B **100**, 77 (2010)

24. Y. Petit, S. Henin, W.M. Nakaema, P. Béjot, A. Jochmann, S.D. Kraft, S. Bock, U. Schramm, K. Stelmaszczyk, P. Rohwetter, J. Kasparian, R. Sauerbrey, L. Wöste, J.-P. Wolf, Phys. Rev. A **83**, 013805 (2011)

25. P. Rairoux, H. Schillinger, S. Niedermeier, M. Rodriguez, F. Ronneberger, R. Sauerbrey, B. Stein, D. Waite, C. Wedekind, H. Wille, L. Wöste, Appl. Phys. B **71**, 573 (2000)

26. R. Bourayou, G. Méjean, J. Kasparian, M. Rodriguez, E. Salmon, J. Yu, H. Lehmann, B. Stecklum, U. Laux, J. Eislöffel, A. Scholz, A.P. Hatzes, R. Sauerbrey, L. Wöste, J.-P. Wolf, J. Opt. Soc. Am. B **22**, 369 (2005)

27. G. Méjean, J. Kasparian, E. Salmon, J. Yu, J.-P. Wolf, R. Bourayou, R. Sauerbrey, M. Rodriguez, L. Wöste, H. Lehmann, B. Stecklum, U. Laux, J. Eislöffel, A. Scholz, A.P. Hatzes, Appl. Phys. B. **77**, 357 (2003)

28. M.C. Galvez, M. Fujita, N. Inoue, R. Moriki, Y. Izawa, C. Yamanaka, Jpn. J. Appl. Phys. **41**, L284 (2002)

29. M. Ferrario, D. Alesini, M. Anania, A. Bacci, M. Bellaveglia, O. Bogdanov, R. Boni, M. Castellano, E. Chiadroni, A. Cianchi, S.B. Dabagov, C. De Martinis, D. Di Giovenale, G. Di Pirro, U. Dosselli, A. Drago, A. Esposito, R. Faccini, A. Gallo, M. Gambaccini, C. Gatti, G. Gatti, A. Ghigo, D. Giulietti, A. Ligidov, P. Londrillo, S. Lupi, A. Mostacci, E. Pace, L. Palumbo, V. Petrillo, R. Pompili, A.R. Rossi, L. Serafini, B. Spataro, P. Tomassini, G. Turchetti, C. Vaccarezza, F. Villa, G. Dattoli, E. Di Palma, L. Giannessi, A. Petralia, C. Ronsivalle, I. Spassovsky, V. Surrenti, L. Gizzi, L. Labate, T. Levato, J.V. Rau, Nucl. Inst. Meth. B **309**, 183 (2013)

30. L.A. Gizzi, F. Anelli, C. Benedetti, C.A. Cecchetti, A. Clozza, G. Di Pirro, N. Drenska, R. Faccini, D. Giulietti, D. Filippetto, S. Fioravanti, A. Gamucci, L. Labate, T. Levato, V. Lollo, P. Londrillo, E. Pace, G. Turchetti, C. Vaccarezza, P. Valente, C. Vicario, II Nuovo Cimento C **32**, 433 (2009)

31. F. Verluise, V. Laude, J.-P. Huignard, P. Tournois, A. Migus, J. Opt. Soc. Am. B **17**, 138–145 (2000)

32. G. Faye, J. Kasparian, R. Sauerbrey, Appl. Phys. B **73**, 157–163 (2001)

33. J. Harms, W. Lahmann, C. Weitkamp, Appl. Opt. **17**, 1131 (1978)

34. J. Harms, Appl. Opt. **18**, 1559 (1978)

35. M. Raymond, *Measures, laser remote sensing, fundamentals and applications* (J. Wiley and Sons, New York, 1984)

36. J. Kasparian, E. Fréjafon, P. Rambaldi, J. Yu, B. Vezin, J.P. Wolf, P. Ritter, P. Viscardi, Atmos. Environ. **32**, 2957–2967 (1998)

37. L. Berge, S. Skupin, G. Mejean, J. Kasparian, J. Yu, S. Frey, E. Salmon, J.-P. Wolf, Phys. Rev. E **71**, 016602 (2005)

38. G. Faye, J. Kasparian, R. Sauerbrey, Appl. Phys. B **73**, 157 (2001)

39. F. Théberge, N. Akozbek, W. Liu, J. Filion, S.L. Chin, Opt. Comm. **276**, 298 (2007)

40. G. Méchain, C. D'Amico, Y.B. André, S. Tzortzakis, M. Franco, B. Prade, A. Mysyrowicz, A. Couairon, E. Salmon, R. Sauerbrey, Opt. Comm. **247**, 171 (2005)

41. M. Rodriguez, R. Bourayou, G. Méjean, J. Kasparian, J. Yu, E. Salmon, A. Scholz, B. Stecklum, J. Eislöffel, U. Laux, A.P. Hatzes, R. Sauerbrey, L. Wöste, J.-P. Wolf, Phys. Rev. E **69**, 036607 (2004)

42. M. Petrarca, S. Henin, K. Stelmaszczyk, S. Bock, S. Kraft, U. Schramm, C. Vaneph, A. Vogel, J. Kasparian, R. Sauerbrey, K. Weber, L. Wöste, J.-P. Wolf, Appl. Phys. Lett. **99**, 141103 (2011)

43. T. Leisner, D. Duft, O. Möhler, H. Saathoff, M. Schnaiter, S. Henin, K. Stelmaszczyk, M. Petrarca, R. Delagrange, Z.Q. Hao, J. Lüder, Y. Petit, P. Rohwetter, J. Kasparian, J.-P. Wolf, L. Wöste, Proc. Natl. Acad. Sci. USA **110**, 10106 (2013)

44. J. Kasparian, P. Rohwetter, L. Wöste, J.-P. Wolf, J. Phys. D Appl. Phys. **45**, 29 (2012)